# An Investigation of the Orthogonal Outputs from an On-rotor MEMS Accelerometer for Reciprocating Compressor Condition Monitoring

G. Feng [a], N. Hu [b], Z. Mones [a], F. Gu [a]*, A.D. Ball [a]

[a] University of Huddersfield, Queensgate, Huddersfield, HD1 3DH, UK

[b] School of Mechatronics Engineering and Automation, National University of Defense Technology, Changsha, Hunan, PR China

**Abstract**

With rapid development in electronics and microelectromechanical systems (MEMS) technology, it becomes possible and attractive to monitor rotor dynamics by directly installing MEMS accelerometers on rotors. This paper studies the mathematical modelling of the orthogonal outputs from an on-rotor MEMS accelerometer and proposes a method to eliminate the gravitational acceleration projected on the measurement axes. This is achieved by shifting the output in the normal direction by $\pi/2$ using a Hilbert transform and then combining it with the output of the tangential direction. With further compensation of the combined signal in the frequency domain, the tangential acceleration of the rotor is reconstructed to a high degree of accuracy. Experimental results show that the crankshaft tangential acceleration of a reciprocating compressor, obtained by the proposed method, can well discriminate different discharge pressures and allow common leakage faults to be detected and diagnosed for online condition monitoring.

**Keywords**: MEMS accelerometer; on-rotor measurement; tangential acceleration; gravitational acceleration cancelation; Hilbert transform

# 1 Introduction

With the recent advancements in electronics and microelectromechanical systems (MEMS) technology, MEMS accelerometers are gaining higher performance profiles at even lower cost. This makes it more attractive to use them as embedded devices for monitoring rotor vibrations more accurately. In particular, it is more convenient to mount them on rotating rotors for the purpose of condition monitoring. In addition, the maturity of low power wireless transmission techniques, such as Zigbee, WirelessHart and Bluetooth Low Energy [1], [2], have made data transmission much more energy efficient and robust. Emerging energy harvesting techniques, such as electro-mechanical and piezoelectric, can harvest energy from the rotational process itself, which offers the potential for the sensor circuit on the rotating body to be battery-less and autonomous [3]–[6].

In recent years, a number of studies have reported the application of using MEMS accelerometers for measuring on-rotor acceleration. As the accelerometer is mounted directly on the rotor, it has the potential to capture the dynamic characteristics of the rotor more accurately [7]. This has been verified by Arebi, et al. [8], in which study a wireless MEMS accelerometer was installed on a rotating shaft to detect shaft misalignments and the results showed that the on-shaft acceleration measurement outperformed the Instantaneous Angular Speed (IAS) acquired from an optical encoder.

*Corresponding author at: University of Huddersfield, Queensgate, Huddersfield, HD13DH, UK.
E-mail address: f.gu@hud.ac.uk (F. Gu).

Elnady et al. [9], used a single on-shaft MEMS accelerometer to replace two or four sensors per bearing for condition monitoring purposes. The reduced number of sensors not only lowers the cost and installation complexity, but also reduces the data analysis burden. Moreover, the investment on sensors can be significantly decreased because the MEMS accelerometer units are increasingly cost-effective due to large scale production for other applications such as smart phones. These attractive advantages have motivated more research in this field. Elnady et al [10] installed a low-weight MEMS accelerometer and a wireless sensor node directly on a shaft to study the critical speeds during machine run-up. Baghli et al. [11] used a MEMS accelerometer to acquire the instantaneous torque and speed on machine shafts. Thompson [4] employed a high-range but low sensitivity MEMS accelerometer to acquire the centrifugal acceleration of a fan blade.

One critical issue in using on-rotor MEMS accelerometers is that the obtained signal contains a combination of gravitational acceleration and rotor dynamic information. The cancelation of the gravitational acceleration by pure post-processing techniques is quite challenging due to the fact that the gravitational acceleration projected on the measurement axis is an angular modulation signal that has the same fundamental frequency as the tangential and centripetal accelerations. In [11], the author mounted two MEMS sensors diametrically opposite on the shaft, to cancel the gravitational acceleration signal. This is a good solution in theory but it requires precise installation of the two sensors, which can be difficult and of course there is the higher cost of using two devices.

This paper studies the mathematical modelling of the orthogonal outputs from an on-rotor MEMS accelerometer and shows that, at higher rotational speeds, the gravitational acceleration signals can be effectively eliminated by combining the phase shifted normal and tangential direction outputs of the MEMS accelerometer. With further compensation of the combined signal in the frequency domain, the tangential acceleration is then reconstructed. Because MEMS accelerometers with two axes or three axes have become commercially common place, the proposed method is relatively easier to implement compared to installing two separate MEMS accelerometers on a rotor.

# 2 Outputs of an On-rotor MEMS Accelerometer

To study the outputs of a MEMS accelerometer mounted on a rotor, two Cartesian coordinate systems are defined in Fig. 1.The first one, denoted $X_O$-$Y_O$-$Z_O$, is a stationary frame to be the reference for any rotating objects including the on-rotor MEMS sensor and the rotor itself. The second is a rotating frame, denoted X-Y-Z, which aligns with the three positive outputs of the MEMS accelerometer at the speed of the rotor. The MEMS accelerometer is fixed on the curved edge of the shaft, normal to the surface, with its Y-direction oriented tangentially. As shown in Fig. 1(a), the MEMS sensor is assumed to have an initial phase $\theta_0$ with respect to the stationary frame. For ease of analysis, the initial phase of any rotational parameter to be measured, such as the angular speed $\omega$, is assumed to be zero with respect to the stationary frame. Thus, $\theta_0$ also represents the phase difference between the sensor and the initial phase of the rotor oscillation.

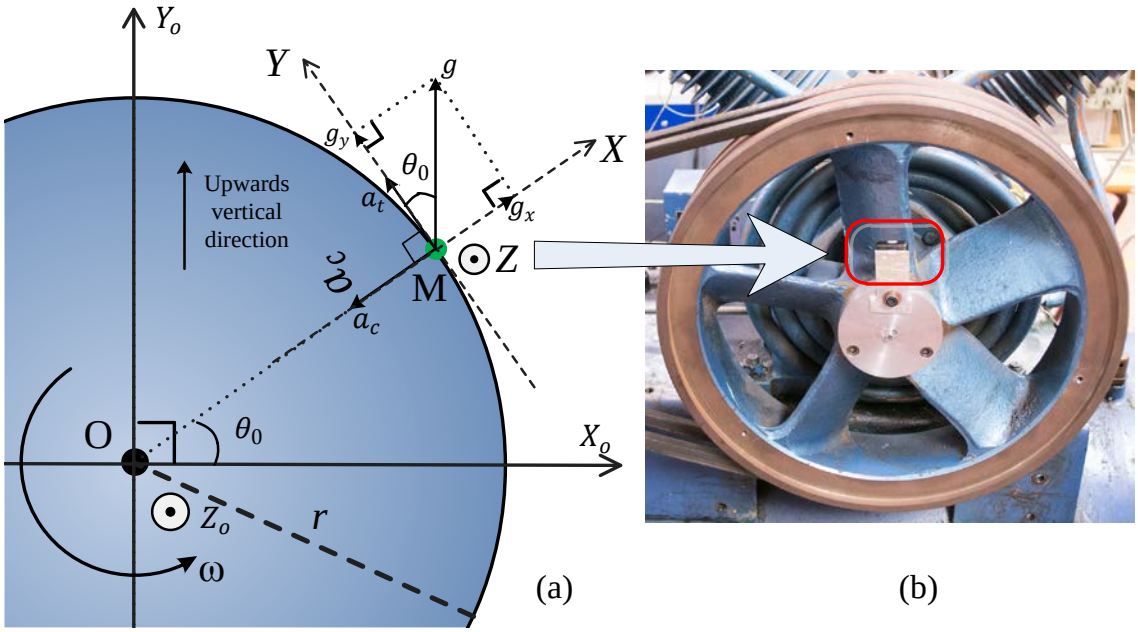


Fig. 1. (a) Acceleration analysis of a mass M rotating around point O and (b) picture of the MEMS sensor installation on the flywheel of the compressor

As the rotor rotates around its centre O, at speed $\omega$, both the centripetal acceleration $a_c$ and the tangential acceleration $a_t$ at radius $r$, can be sensed by the MEMS accelerometer in the X- and Y-direction, respectively. In addition, the accelerometer can sense the acceleration from gravity. In the gravity field, an acceleration of 1.0g, but with an opposite direction to the earth's gravity, can be sensed by accelerometer [12]. This means that there is always an acceleration vertically upwards with amplitude of 1.0g as shown in Fig. 1(a). When the rotor rotates, this acceleration from gravity will project onto the X- and Y-axes of the sensor. Therefore, the outputs of the sensor are:

$$a_x = -a_c + g_x \tag{1}$$

$$a_y = a_t + g_y \tag{2}$$

where $g_x$ and $g_y$ denote the gravitational acceleration projected on the X- and Y-axes, respectively. This reveals that the measured signals consist not only of the desired rotational motion components, which reflect the rotor dynamics, but also the inherent gravitational acceleration which effectively interferes with the sensor measurements. Obviously, the latter has to be eliminated, or at least minimised, in the measurements to enable the true dynamic behaviour of the rotor to be reflected in the signal.

## 2.1 Centripetal and Tangential Accelerations

As the rotor rotates at a time-varying speed $\omega$, associated with angular acceleration $\alpha = d\omega/dt$, the centripetal acceleration $a_c$ and tangential acceleration $a_t$ are as follows:

$$a_c = \omega^2 r \tag{3}$$

$$a_t = \alpha r \tag{4}$$

Supposing that the angular speed to be measured is $\omega = \omega_0 + \tilde{\omega}$, where $\omega_0$ represents the steady angular speed and $\tilde{\omega}$ is the dynamic angular speed (i.e. its amplitude varies with time), the centripetal acceleration $a_c$ and tangential acceleration $a_t$ can be written:

$$a_c = (\omega_0 + \tilde{\omega})^2 r = r\omega_0^2 + 2r\omega_0\tilde{\omega} + r\tilde{\omega}^2 \tag{5}$$

$$a_t = r\frac{d\tilde{\omega}}{dt} \tag{6}$$

In the vast majority of general machine applications, rotational speed fluctuations of a rotor is small compared to the underlying speed, e.g. a typical induction motor drive experiences slip of no more than 5% [13]. This means that the speed of a typical induction motor drive oscillates less than 5% around its rated speed, thus it is acceptable that $\tilde{\omega}/\omega_0 \ll 1$. On this basis, the quadratic term $r\tilde{\omega}^2$ is negligible. In addition, the steady component $r\omega_0^2$ is of minimal interest for dynamic analysis. So the dynamic centripetal acceleration $\tilde{a}_c$ in (5) can be approximated as:

$$\tilde{a}_c \approx 2r\omega_0\tilde{\omega} \tag{7}$$

Furthermore, the dynamic angular speed can be considered as a periodic signal which can be expanded as a Fourier series:

$$\tilde{\omega} = \sum_{n=1}^{\infty} A_n \sin(n\omega_p t + \varphi_n) \tag{8}$$

where $A_n$ and $\varphi_n$ represent the amplitude and phase of the $n^{th}$ component in $\tilde{\omega}$ respectively, and $\omega_p$ is the fundamental frequency of the periodic signal. For many rotating processes, $\omega_p$ can be the steady angular speed $\omega_0$ due to the effect of misaligned shafts, imbalanced rotors and such. The dynamic angular speed $\tilde{\omega}$ can thus be written:

$$\tilde{\omega} = \sum_{n=1}^{\infty} A_n \sin(n\omega_0 t + \varphi_n) \tag{9}$$

On this basis, the dynamic centripetal acceleration $\tilde{a}_c$ and tangential acceleration $\tilde{a}_t$ can be expressed as the combination of the harmonics of the fundamental components:

$$\tilde{a}_c \approx \sum_{n=1}^{\infty} 2r\omega_0 A_n \sin(n\omega_0 t + \varphi_n) \tag{10}$$

$$\tilde{a}_t = \sum_{n=1}^{\infty} nr\omega_0 A_n \cos(n\omega_0 t + \varphi_n) \tag{11}$$

## 2.2 Gravitational Acceleration Projection Signals

As shown in Fig. 1, the gravitational acceleration projection on the X-axis ($g_x$) and Y-axis ($g_y$) can be expressed:

$$g_x = g\sin\theta \tag{12}$$

$$g_y = g\cos\theta \tag{13}$$

where $\theta$ is the total angular displacement for the sensor at time $t$ and is related to the angular speed by:

$$\theta = \theta_0 + \int_0^t \omega dt \tag{14}$$

Considering that the angular speed is composed of both steady component $\omega_0$ and dynamic component $\tilde{\omega}$, the total angular displacement of the sensor at time $t$ is:

$$\begin{aligned} \theta &= \theta_0 + \int_0^t (\omega_0 + \tilde{\omega}) dt \\ &= \theta_0 + \omega_0 t + \int_0^t \tilde{\omega} dt \end{aligned} \tag{15}$$

This shows that the total angular displacement is comprised of three components: the initial angular displacement $\theta_0$, the linear progression displacement due to steady speed $\omega_0$ and the oscillated angular displacement due to dynamic angular speed $\tilde{\omega}$. Let the third component displacement oscillation defined as $\phi(t)$ and expanded:

$$\phi(t) = \int_0^t \tilde{\omega} dt = \frac{1}{\omega_0} \sum_{n=1}^{\infty} \frac{A_n}{n} [-\cos(n\omega_0 t + \varphi_n) + \cos\varphi_n] \tag{16}$$

It can be seen that the projections in (12) and (13) are pure sinusoidal waveforms on the condition that the dynamic angular speed $\tilde{\omega} = 0$ and $\phi(t) = 0$. In practice, there always exist a small dynamic angular speed $\tilde{\omega}$ which produces a small oscillation angular displacement $\phi(t)$. Because of the small oscillation $\phi(t)$, the projections in (12) and (13) may have a large number of higher order components due to angular modulation effect. However, considering that the amplitude of $\phi(t)$ is usually small compared to that of the steady angular speed, (which is typical for many machines such as pumps, engines and compressors), only the significant linear term of $\phi(t)$ needs to be taken into account in the derivation of the projections, leading to:

$$\begin{aligned} g_x &= g sin[\theta_0 + \omega_0 t + \phi(t)] \\ &\approx g\sin(\theta_0 + \omega_0 t) + g\phi(t)\cos(\theta_0 + \omega_0 t) \end{aligned} \tag{17}$$

$$\begin{aligned} g_y &= g cos[\theta_0 + \omega_0 t + \phi(t)] \\ &\approx g\cos(\theta_0 + \omega_0 t) - g\phi(t)\sin(\theta_0 + \omega_0 t) \end{aligned} \tag{18}$$

This show that $g_x$ and $g_y$ consist not only of a carrier signal with amplitude $g$ and frequency $\omega_0$ but also a series of small sidebands, which have a $\pi/2$ phase shift with respect to the carrier. The amplitude of the sidebands can be determined by $\phi(t)$ in (16). Substituting $\phi(t)$ from (16) into (17) and (18), $g_x$ and $g_y$ can be expanded as follows:

$$g_x \approx g\sin(\theta_0 + \omega_0 t) + \frac{g}{\omega_0}\sum_{n=1}^{\infty}\frac{A_n}{n}\left\{-\frac{1}{2}\cos[(n+1)\omega_0 t + \theta_0 + \varphi_n] - \frac{1}{2}\cos[(1-n)\omega_0 t + \theta_0 - \varphi_n] + \cos\varphi_n \cos(\theta_0 + \omega_0 t)\right\} \quad (19)$$

$$g_y \approx g\cos(\theta_0 + \omega_0 t) + \frac{g}{\omega_0}\sum_{n=1}^{\infty}\frac{A_n}{n}\left\{\frac{1}{2}\sin[(n+1)\omega_0 t + \theta_0 + \varphi_n] + \frac{1}{2}\sin[(1-n)\omega_0 t + \theta_0 - \varphi_n] - \cos\varphi_n \sin(\theta_0 + \omega_0 t)\right\} \quad (20)$$

Due to the nonlinear angular modulation process, the n[th] harmonic in the dynamic angular speed $\tilde{\omega}$ generates three significant frequency components in both $g_x$ and $g_y$, which are $(n+1)\omega_0$, $(n-1)\omega_0$ and $\omega_0$. Of note, $g_x$ and $g_y$ have the same amplitude for all frequency components whilst exhibiting a phase difference of $\pi/2$.

## 2.3 Tangential Acceleration Reconstruction

Substituting (10) and (11), into (1) and (2) respectively gives the approximate outputs in the X- and Y- axes:

$$\tilde{a}_x = -\tilde{a}_c + g_x \approx -\sum_{n=1}^{\infty} 2r\omega_0 A_n \sin(n\omega_0 t + \varphi_n) + g_x \quad (21)$$

$$\tilde{a}_y = \tilde{a}_t + g_y \approx \sum_{n=1}^{\infty} nr\omega_0 A_n \cos(n\omega_0 t + \varphi_n) + g_y \quad (22)$$

It can be seen that the sensor outputs in both X- and Y-axis are mixed with the gravitational accelerations. According to the definitions in (19) and (20), the gravitational accelerations are influenced not only by the rotational process but also the initial phase $\theta_0$ relevant to the angular displacement of the installation position. This makes them rather complicated and thus are intended to be eliminated from the sensor outputs.

From (19) and (20), it is found that all frequency components in $g_x$ and $g_y$ have the same amplitude but have a phase difference of $\pi/2$. This means the gravitational projection in one axis can be eliminated by adding/subtracting the $\pi/2$ phase shifted version of the gravitational projection in the other axis. Hilbert transform ~~is such a effective transform that~~ can shift a signal by $\pi/2$ [14] and can be implemented easily in the frequency domain. T~~t~~hereafter can be employed to process the signal. With an observation on the other components in $\tilde{a}_x$ and $\tilde{a}_y$, i.e. $-\tilde{a}_c$ and $\tilde{a}_t$, interestingly, their corresponding frequency components also have a fixed phase difference of $\pi/2$ but have different amplitudes. This special feature of the sensor outputs has entitled the Hilbert transform method suitable for eliminating the gravitational acceleration projections.

On this basis, a method is hereby proposed to cancel the gravitational acceleration projection on the Y-axis, i.e. $g_y$, thus permitting the tangential acceleration of interest to be reconstructed. Below are the reconstruction steps:

1) Apply a low-pass filter to both $\tilde{a}_x$ and $\tilde{a}_y$ to remove the high frequency noise whilst retaining the first four harmonics;
2) Apply a phase shift of $\pi/2$ to the filtered signal $\tilde{a}_x$ using a Hilbert transform [14]; and
3) Add the phase shifted signal to the filtered signal $\tilde{a}_y$, resulting in a signal that excludes gravitational components and only comprises the tangential acceleration components:

$$a_{tx} = \sum_{n=1}^{4} (n+2) r \omega_0 A_n \cos(n\omega_0 t + \varphi_n) \tag{23}$$

Comparing (23) with $\tilde{a}_t$ in (11), it can be seen that the frequency contents and phases are very similar but that the amplitude of the n[th] harmonic component is $(n+2)/n$ times that of the true one. Clearly, it is straightforward to correct this constant difference in the frequency domain and hence to obtain the true tangential acceleration of interest. Therefore, it is feasible to use the orthogonal outputs of the on-rotor MEMS accelerometer to eliminate the effect of gravitational acceleration and so to reconstruct the desired tangential acceleration for rotor dynamic analysis.

# 3 Performance analysis

This section uses a real rotor system of two-stage reciprocating compressor to validate the performance of the reconstruction method derived in Section 2. The rotor system is simulated and the related acceleration signals are calculated according to the equations given in (1) - (4), (12) and (13). Based on this, the performance of the reconstruction method is examined under a range of real operating conditions. In the following section (Section 4), the experimental validation of the method is reported along with the specifications of the real machine.

## 3.1 Reconstruction Method Verification

The compressor rotor rotates at around 440 rpm (7.3 Hz). Due to the reciprocating motion of the pistons, a relatively high speed fluctuation ratio of 5% is assumed for this analysis [15], meaning that the amplitude of the dynamic component of angular speed will be around $440 \times 5\% = 22$ rpm (0.37 Hz). In addition, three higher orders of harmonics are introduced to represent the nonlinear torque due to air compression and piston motion. Specially, the angular speed of the crankshaft is simulated by:

$$\omega = \frac{2\pi}{60}\left[440t + 20\sin\left(2\pi\frac{440}{60}t + \frac{\pi}{3}\right) + 8\sin\left(4\pi\frac{440}{60}t + \frac{\pi}{2}\right) + 5\sin\left(6\pi\frac{440}{60}t + \frac{2\pi}{3}\right) + 2\sin\left(8\pi\frac{440}{60}t + \frac{3\pi}{4}\right)\right] \tag{24}$$

As shown in Fig. 2, the speed oscillates with not only the dominant content of the 1st harmonic but also the observable components at the 2nd, 3rd and 4th harmonics, revealing the general motion dynamics of a compressor with two pistons.

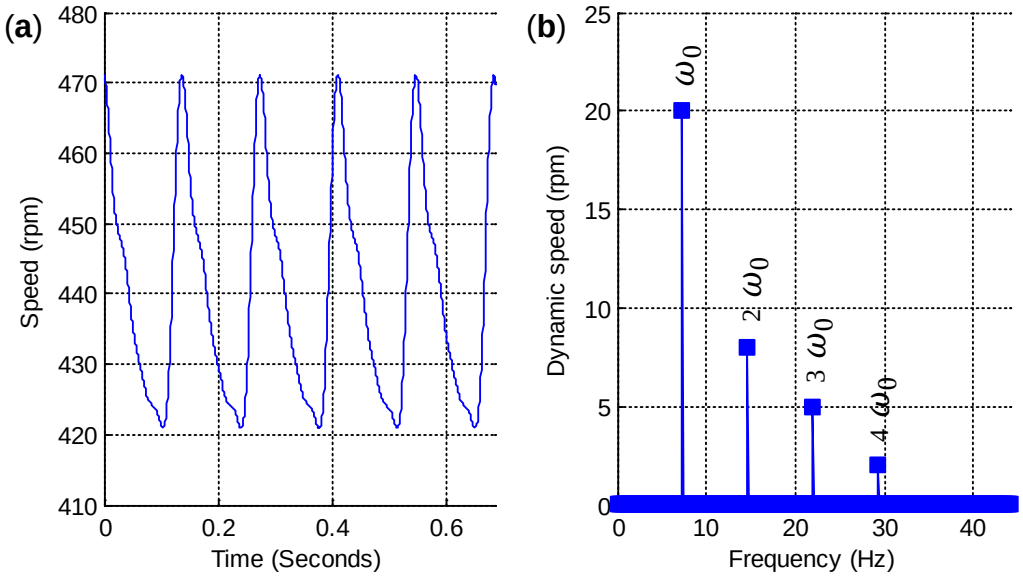


Fig. 2. (a) Angular speed signal in time domain and (b) spectrum of the dynamic angular speed

Taking the radius $r$ of the sensor location to be 0.05m, and the initial angular displacement $\theta_0$ as 0 with the angular speed signal in Fig. 2(a) as the input, the dynamic centripetal acceleration $\tilde{a}_c$, tangential acceleration $\tilde{a}_t$, and gravitational acceleration projections $g_x$ and $g_y$ can be calculated according to the modelling in Section 2. As shown in Fig. 3 (a) and (b), both the dynamic centripetal acceleration $\tilde{a}_c$ and tangential acceleration $\tilde{a}_t$ show clearly the frequency content corresponding to the input angular speed ω. However, because of nonlinear effects, $\tilde{a}_c$ contains quadratic amplitude variation in addition to higher order components. This means that $\tilde{a}_c$ cannot be used as a basis for constructing rotational dynamics, whereas $\tilde{a}_t$ (in which the components are linearly correlated with speed oscillations) can be used for constructing the fluctuations.

The gravitational acceleration projections $g_x$ and $g_y$, shown in Fig. 3 (c) and (d) respectively, exhibit unity g components at the fundamental frequency. However, it is hard to see the sidebands caused by the angular modulation. Meaning that it is acceptable to approximate $g_x$ and $g_y$ in (19) and (20) by simply considering the significant linear term of $\phi(t)$.

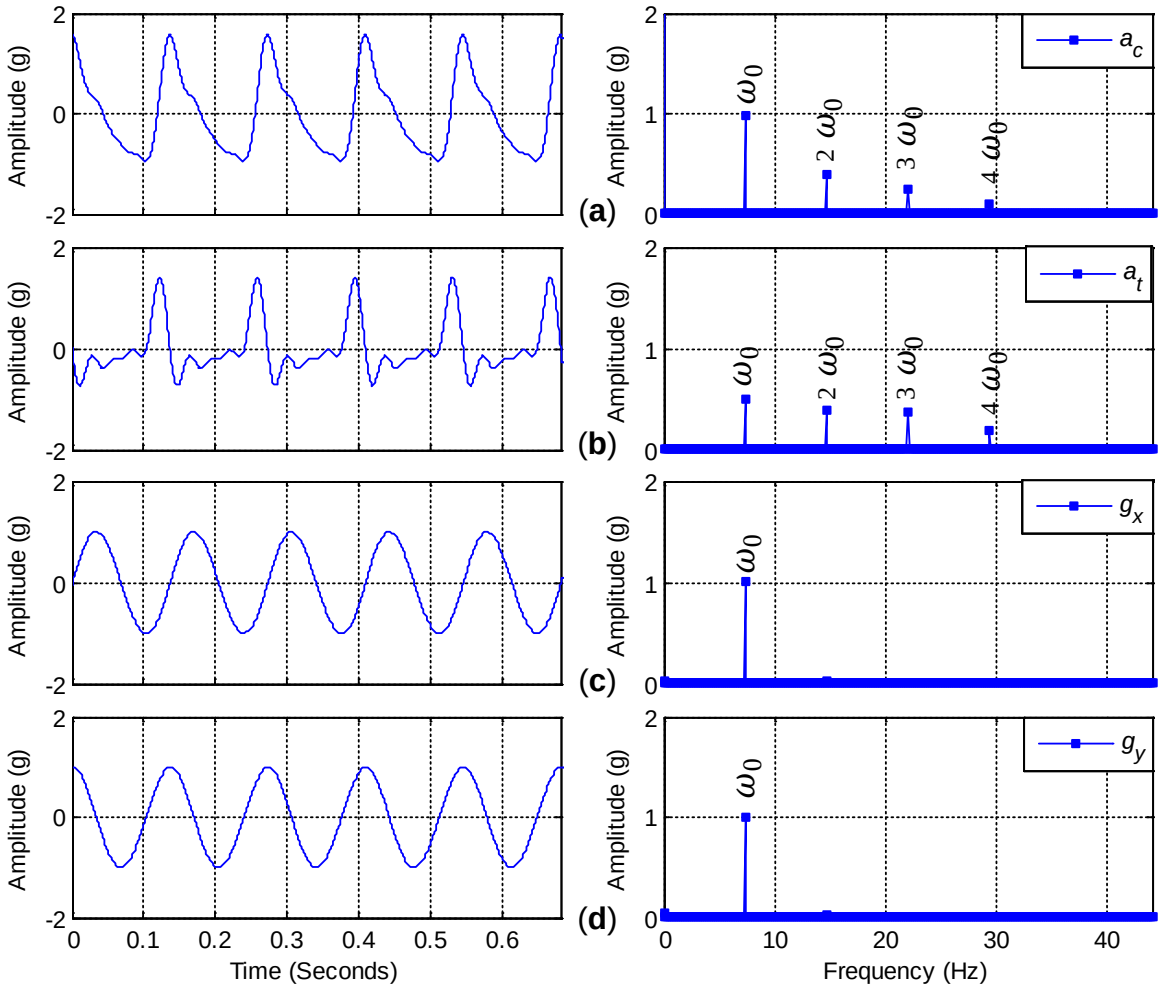


Fig. 3. True accelerations and their spectra (a) centripetal acceleration $\tilde{a}_c$, (b) tangential acceleration $\tilde{a}_t$, (c) gravitational acceleration projection on X-axis $g_x$ and (d) gravitational acceleration projection on Y-axis $g_y$.

By substituting the calculated accelerations $\tilde{a}_c$, $\tilde{a}_t$, $g_x$ and $g_y$ into expressions (1) and (2), the sensor output signals for the X-axis ($a_x$) and Y-axis ($a_y$) can be computed and are shown in Fig. 4 (a) and (b), respectively. It can be seen that $a_x$ and $a_y$ exhibit predominant oscillation according to the fundamental frequency. However they exhibit significant differences from $\tilde{a}_c$ and $\tilde{a}_t$ in Fig. 3 (a) and (b) because of their combination with the gravitational acceleration projections. In particular, the spectral component at the fundamental frequency for $a_x$ is slightly larger than 1g whereas for $a_y$ it is much larger, due to the superposition of rotor oscillation and gravitational effects. Furthermore, the higher order harmonics of $a_x$ and $a_y$ are consistent with those of $\tilde{a}_c$ and $\tilde{a}_t$, respectively, showing that the sensor output contains the full information of the speed fluctuation.

To recover the tangential acceleration, the previously proposed reconstruction method is applied to the outputs $a_x$ and $a_y$ to obtain $\tilde{a}_{tr}$. Fig. 4 (c) shows a comparison between the reconstructed signal $\tilde{a}_{tr}$ and the true tangential acceleration $\tilde{a}_t$. It can be seen that these two signals are very similar in both the time and frequency domains, validating the reconstruction method.

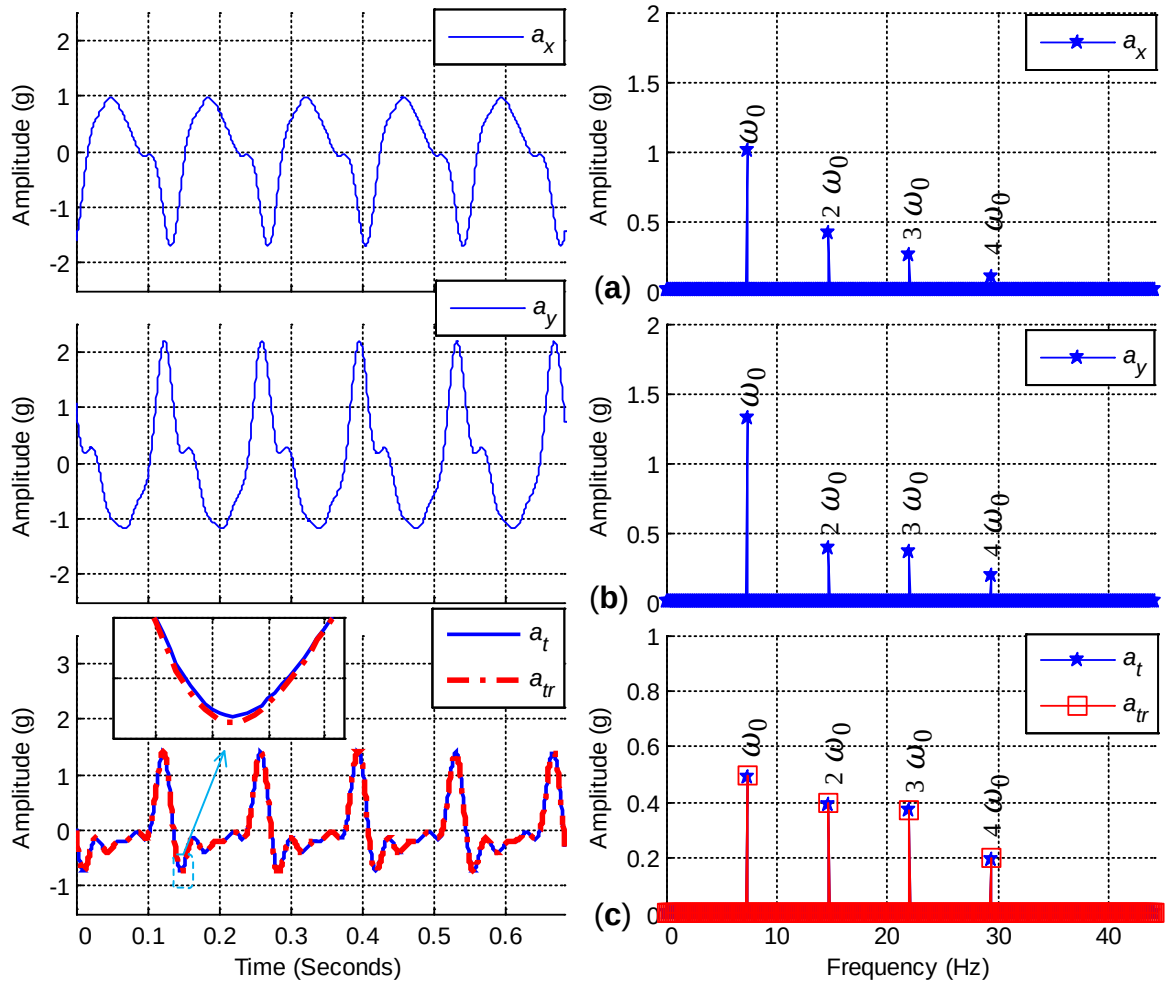


Fig. 4. Processed signals and their spectra (a) signal in X-axis $\tilde{a}_x$, (b) signal in Y-axis $\tilde{a}_y$ and (c) true tangential signal $\tilde{a}_t$ and reconstructed signal $\tilde{a}_{tr}$ with magnified portion shown as an inset

## 3.2 Error Analysis

To explore in more detail of the reconstruction performance, the four harmonics can be extracted from the spectra in Fig. 4 (c) and then compared with their original values. Table 1 shows the comparison results. It reveals that the absolute errors of the reconstructed signals for all the four harmonics are of similar magnitude and relatively small. Overall, the reconstruction errors are deemed to be acceptable because their absolute values are close to the resolution of the sensor employed in the experimental test (see Section 4.1). It would seem that the accuracy is mainly limited by the sensor resolution, making the reconstruction error insignificant.

Table 1 Harmonic comparison between $\tilde{a}_t$ and $\tilde{a}_{tr}$ in Fig. 4(c)

| | First harmonic | Second harmonic | Third harmonic | Fourth harmonic |
|---|---|---|---|---|
| Amplitude of $\tilde{a}_t$ (g) | 0.4918 | 0.3934 | 0.3687 | 0.1966 |
| Amplitude of $\tilde{a}_{tr}$ (g) | 0.4939 | 0.3974 | 0.3725 | 0.2002 |
| Error (g) | -0.0020 | -0.0040 | -0.0037 | -0.0037 |

Note: Resolution of the MEMS accelerometer in the experimental test is 0.0039g/LSB.

To examine the error distributions under different rotor dynamic characteristics, a Monte-Carlo test was performed based on the general form of the angular speed in (24). In the test, the amplitudes of the harmonics of $\tilde{\omega}$ were made to be random values with ranges listed in Table 2, but following an approximate relationship where $A_1 > A_2 > A_3 > A_4$. In addition, the initial phase $\varphi_n$ $(n = 1,2,3,4)$ and initial angular displacement $\theta_0$ were set to random values between 0 and $2\pi$. These inputs allowed exploratory speed fluctuations to be generated and corresponding reconstruction errors to be calculated. After 10,000 iterations, the errors for the four harmonics are shown in Table 3. Even in extreme cases, the construction errors are only a small number of multiples of the sensor resolution, demonstrating that the influence of the approximation is limited and hence that the reconstruction method is robust.

Table 2 Parameter ranges for the Monte-Carlo simulation

| Parameters | $A_1$ | $A_2$ | $A_3$ | $A_4$ | $\theta_0, \varphi_1, \varphi_2, \varphi_3, \varphi_4$ |
|---|---|---|---|---|---|
| Uniform range | [10, 20] rpm | [6, 12] rpm | [3, 8] rpm | [1, 4] rpm | $[0 \sim 2\pi]$ |

Table 3 Error results of the Monte-Carlo test

| | First harmonic | Second harmonic | Third harmonic | Fourth harmonic |
|---|---|---|---|---|
| Lower error bound (g) | -0.0108 | -0.0133 | -0.0096 | -0.0081 |
| Upper error bound (g) | 0.0082 | 0.0114 | 0.0102 | 0.0080 |
| Error range (g) | 0.0190 | 0.0247 | 0.0198 | 0.0161 |

# 4 Case Study

## 4.1 Experimental Setup

To evaluate the performance when using the reconstructed signals for condition monitoring, an experimental study was performed on a two-stage, single-acting Broom Wade reciprocating compressor (Model TS9). A schematic of the compressor is illustrated in Fig. 5 (a). The compressor consists of three fundamental parts, an electric motor, a two-cylinder compression unit and a high pressure receiver (tank) that stores the compressed air [15]. The compression unit is composed of two cylinders, two pistons, two connecting rods, a crankshaft, four self-acting valves and an intercooler. The compressor is driven by a three phase 2.5 kW induction motor KX-C184, whose power is transferred to the flywheel through a multi-belt pulley system with a transmission ratio of 3.2:1. The rated speed of the motor is 1420 rpm, thus the rated speed of the flywheel is about 440 rpm. The compressor delivers compressed air between 0.55 MPa (80 psi) and 0.83 MPa (120 psi) to a horizontal air tank with a maximum working pressure of 1.38MPa (200 psi).

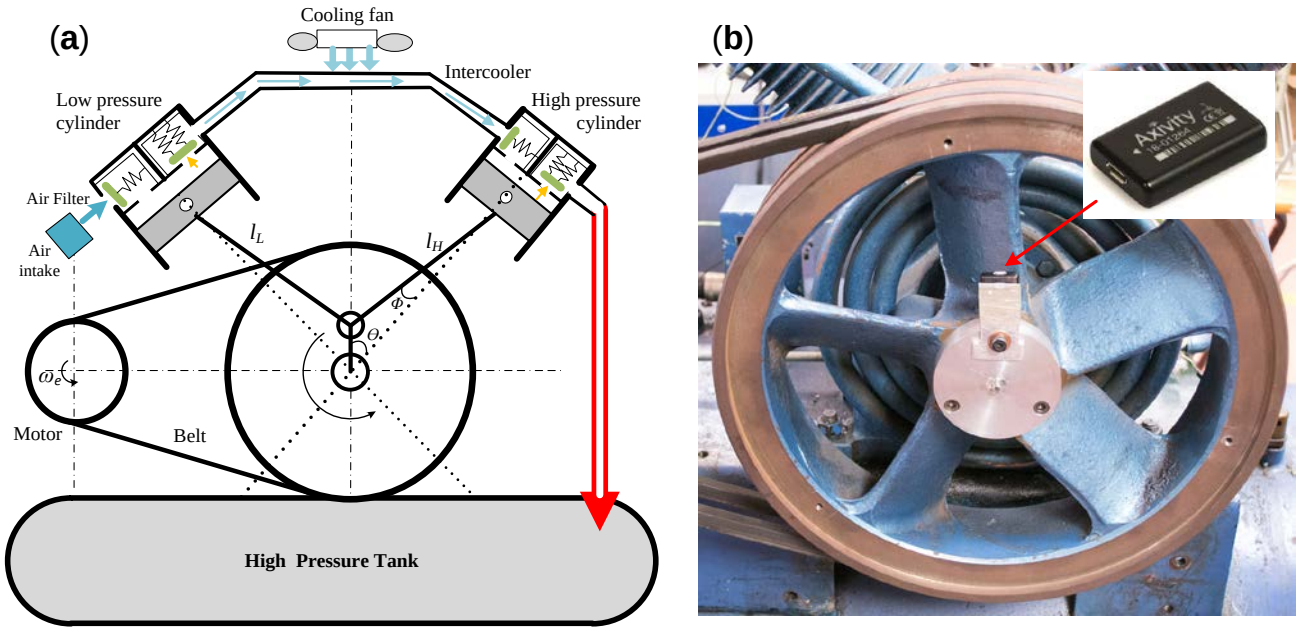


Fig. 5. (a) Schematic diagram of a two-stage reciprocating compressor and (b) installation of MEMS accelerometer on the flywheel of the test compressor

A three axis MEMS acceleration data logger AX3 from Axivity [16] is mounted close to the centre of the flywheel to record the on-rotor accelerations, as illustrated in Fig. 5 (b). Since the centripetal acceleration has a squared relationship with the steady angular speed, the data logger is set with approximately 50 mm offset from the shaft centre to allow the full waveform of the centripetal acceleration to be within its dynamic range. The specification of the AX3 data logger is listed in Table 4. During the test, it is configured to operate with a dynamic range of ±16g and a sampling rate of 1600Hz to allow sufficient rotor dynamic information to be acquired. The recorded data is stored in memory during machine run-time and thereafter exported for post-processing after the machine is shut down. Simultaneously, the tank pressure is also recorded via a data acquisition system, to act as a load reference for post processing.

Table 4 Specification of Axivity AX3 data logger

| | |
|---|---|
| **Memory** | 512Mb flash non-volatile |
| **Accelerometer sample rate** | 12.5 - 3200Hz configurable |
| **Battery life** | 30 days @ 12.5Hz; 14 days @ 100Hz |
| **Accelerometer range** | ±2 / 4 / 8 / 16g configurable |
| **Accelerometer resolution** | Up to 13 bit (0.0039g/LSB) |
| **Dimensions** | 23 x 32.5 x 7.6 (mm) |
| **Weight** | 11g |

## 4.2 Baselining

To show the basic characteristics of the measured signals, Fig. 6 presents a typical set of sensor outputs when the compressor operates at 0.55 MPa (80 psi). This shows that the acceleration signals in both the X- and Y-axes exhibit periodic oscillations correlated to the rotational speed of the crank,

showing the fundamental dynamics of the compressor operation. However, there is a distinctive negative offset observed in the X-axis, which is due to the centripetal acceleration. In addition, a less significant negative offset is also observable on the acceleration in the Y-axis, which is the projection of the centripetal acceleration due to the sensor not being strictly aligned with the tangential direction of the rotation. Neither of these DC offsets is of interest for dynamic analysis because it contains no time varying information.

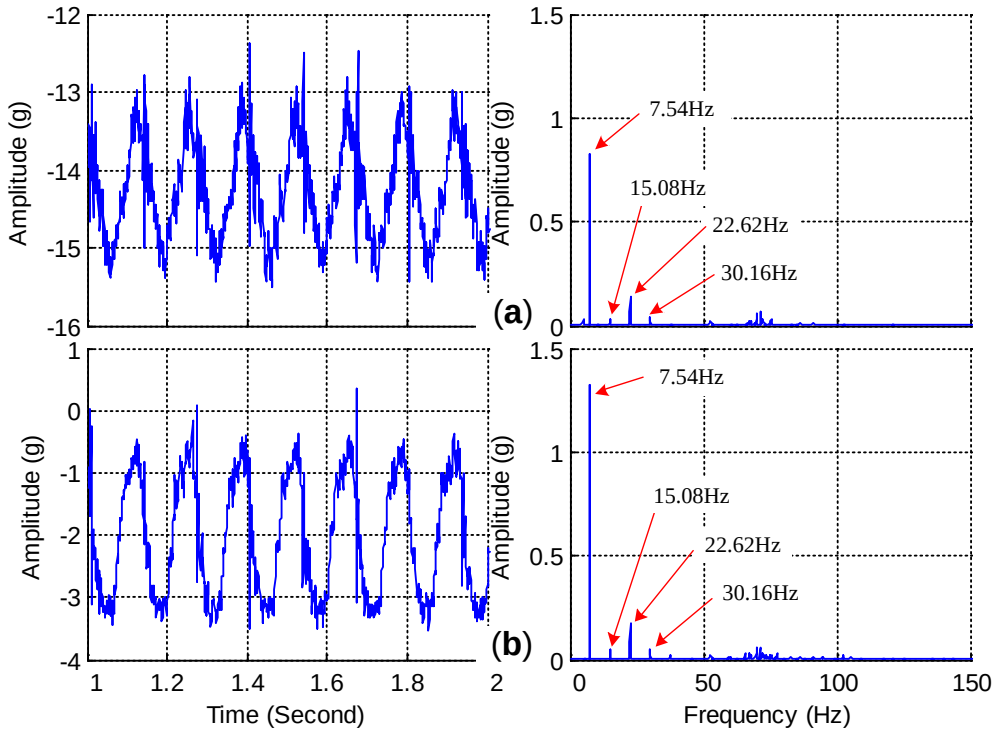


Fig. 6. Acceleration signals and their spectra at a pressure of 0.55 MPa (80 psi) (a) X-axis and (b) Y-axis

The spectra in Fig. 6 show clearly that the largest frequency components for both of the two channels are situated at 7.54 Hz, i.e. the steady angular speed of the crank shaft, and this value is taken as the fundamental frequency. In addition, there are at least 4 higher harmonics that are pertinent to the compressor dynamics. A number of higher frequency components can also be observed above 50Hz. These are from structural vibrations and are not of interest to our analysis. After removing these components using a low pass filter, the tangential acceleration is reconstructed using the proposed reconstruction method. As shown in Fig. 7, the tangential acceleration is mainly composed of the fundamental and its three higher harmonic frequency components. Comparatively, the fundamental frequency component is the largest one and the third harmonic is much higher than the $2^{nd}$ and $4^{th}$ harmonics, showing the general dynamic characteristics of the crankshaft due to the combination of air pressure fluctuation and reciprocating inertia [14].

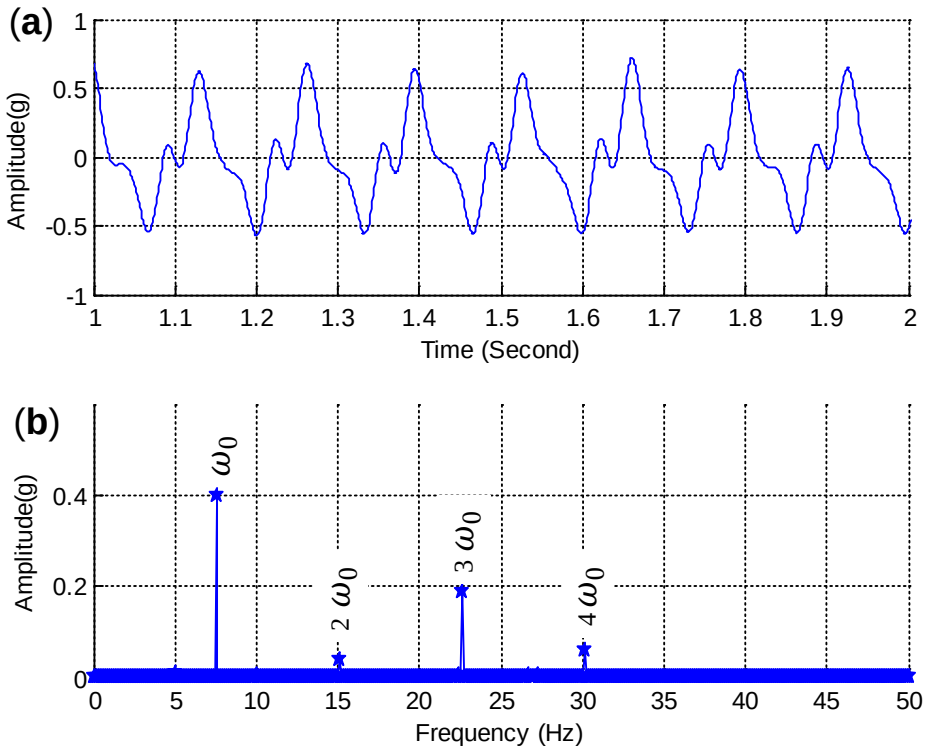


Fig. 7. Tangential acceleration with tank pressure of 0.55 MPa (80 psi), (a) time domain and (b) frequency domain

To confirm that the identified features are general dynamic characteristics, the reconstructed signals for different tank pressures are presented in Fig. 8. It can be seen that the fundamental frequency component and the 3rd and 4th harmonics exhibit linear correlations with pressure over the entire pressure range, reflecting the effect of pressure induced torque. However, the 2nd harmonic shows a nonlinear correlation with pressure which reflects the effect of the torque due to the inertia of reciprocating mass. Moreover, the fundamental and the 3rd harmonic show relatively higher amplitude and can discriminate between successive changes in pressure. The results in Fig. 8 underline that the extracted features have good signal to noise ratios and are sufficiently sensitive to show small changes in pressure. They are hence deemed to be reliable indicators of compressor dynamics.

The variation of harmonics with pressure is noticeably quite smooth and there are no large jumps between successive pressure steps. This indicates that the sensor system and reconstruction method perform reliably even if the compressor has high overall vibration levels.

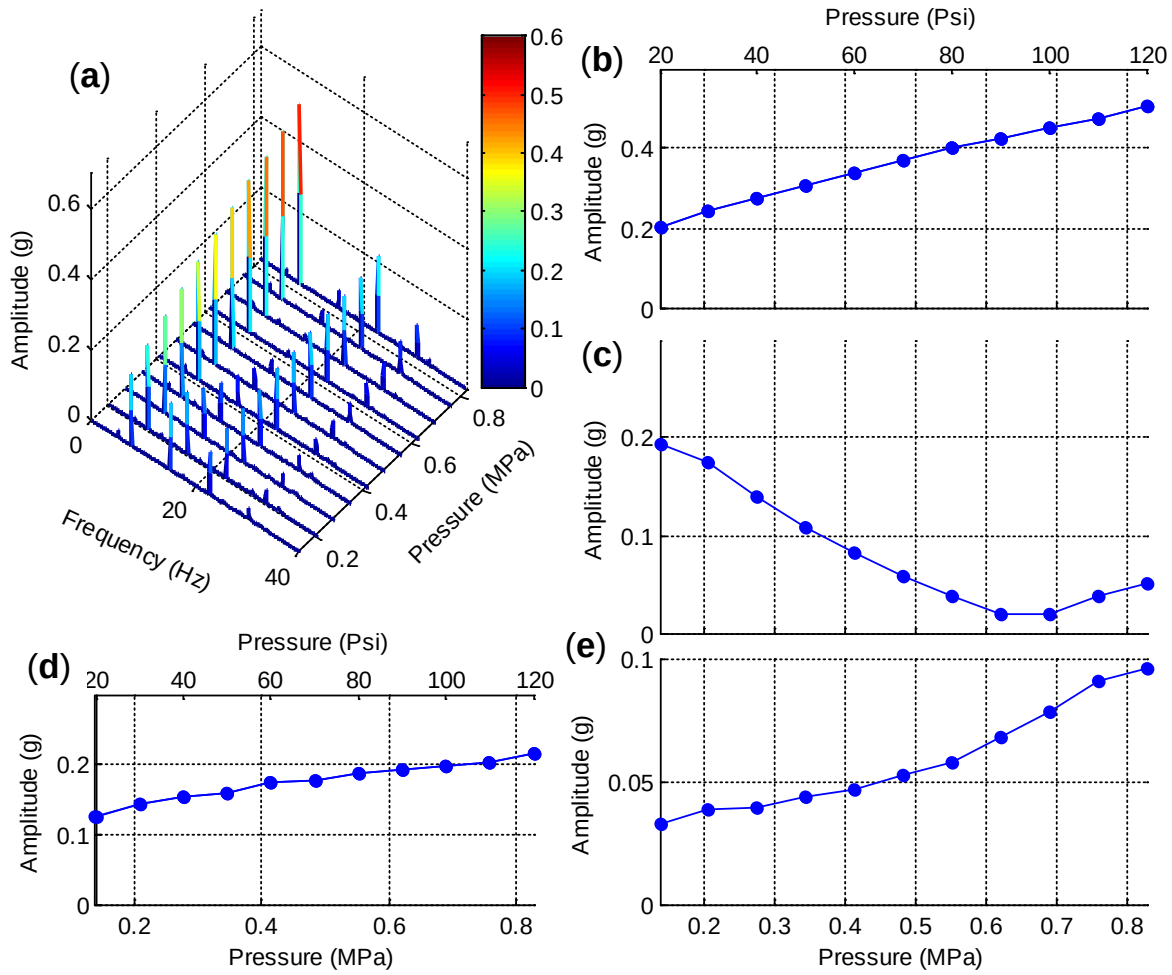


Fig. 8. Spectral features of tangential acceleration under tank pressures from 0.14 MPa (20 psi) to 0.83 MPa (120 psi), (a) spectra as a waterfall plot, (b) amplitude of fundamental frequency, (c) amplitude of 2nd harmonic, (d) amplitude of 3rd harmonic and (e) amplitude of 4th harmonic

## 4.3 Leakage Signals

To evaluate further the performance of the proposed method, more measurements were obtained with the compressor in a range of induced common faults. As shown in Table 5, the faults (which were simulated one by one) include one very small intercooler leakage (IL1) and one minor intercooler leakage (IL2), which were simulated by loosening the intercooler with two degrees of severity, one minor discharge valve leakage on the high pressure cylinder (VL) which was produced by creating a 2 mm diameter hole in the discharge valve plate, and a combination fault (IL2+VL) comprised of the minor intercooler leakage and the discharge valve leakage fault introduced simultaneously. All of these faults only caused minor changes to the overall performance of the compressor and their presence is difficult to be identified from operating parameters, as shown in Fig. 9 where the time durations of charging the pressure vessel exhibit small differences between fault cases and healthy condition.

Table 5 Fault cases

| Test case | Description |
|---|---|
| **BL** | Baseline signal (healthy) |
| **IL1** | Very small intercooler leakage |
| **IL2** | Minor intercooler leakage |
| **VL** | Minor discharge valve leakage on the high pressure cylinder |
| **IL2+ VL** | Minor intercooler leakage + minor discharge valve leakage on the high pressure cylinder |

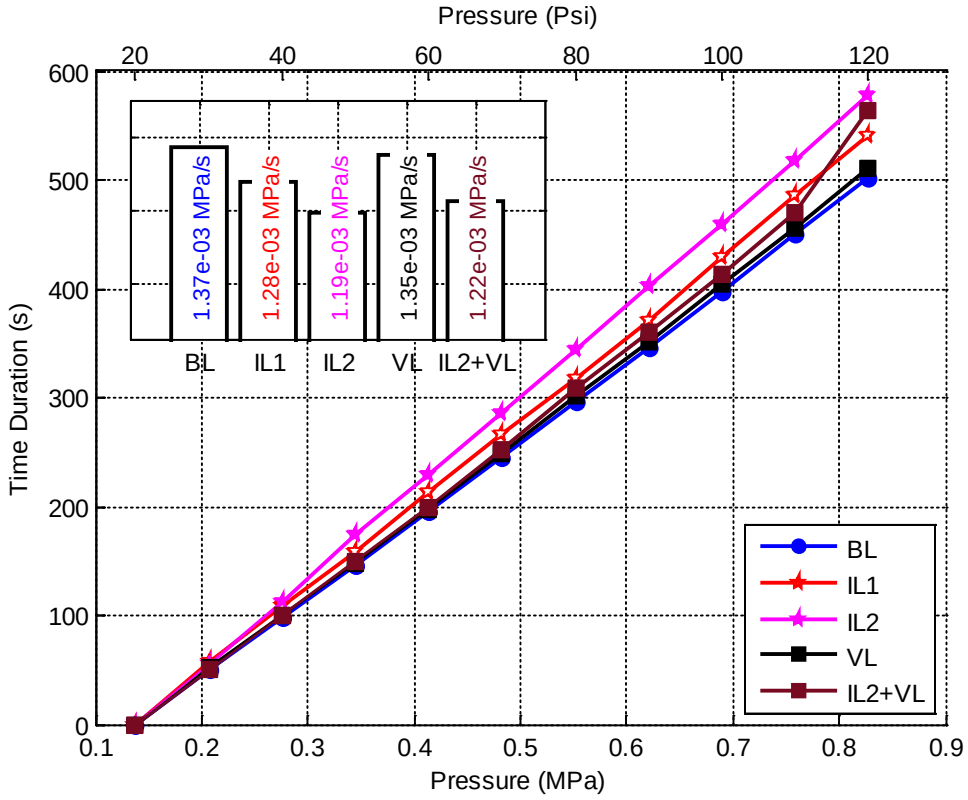


Fig. 9. Time to charge pressure vessel comparison for different fault conditions with average pressure increase rate shown as inset

Fig. 10 shows a comparison of the tangential accelerations for different fault cases including the baseline. Similar to the baseline signal, the fundamental and third harmonic components show a clear linear increasing trend in all fault cases over the entire discharge pressure range. However, their increasing slopes show small differences between different cases. Particularly, the valve leakage fault case (VL) and the combined fault case (IL2+VL) produce more rapidly rising slopes compared to the baseline case, whereas the two intercooler leakage cases (IL1 and IL2) cause slower increase in the harmonic components. It can hence be seen that the first and third harmonics are useful for reflecting the pressure and their features can be employed to classify the leakage fault cases. In contrast, the second harmonic shows distinctive difference between fault cases at a given pressure, however, this relationship is nonlinear and thus not straightforward for classification. For the fourth harmonic, the amplitudes are rather small, being close to the resolution of the MEMS accelerometer (0.0039g/LSB), which makes it unsuitable for use in fault classification.

The relationship of the 3rd harmonic with the fundamental component, for discharge pressure in the range 0.41 MPa (60 psi) to 0.83 MPa (120 psi) is presented in Fig. 11 (a). Based on this, the fault signals are classified in Fig. 11 (b). This shows that the intercooler faults (IL1 and IL2) and the discharge valve leakage fault (VL) can be well separated from the baseline signal (BL). Specifically, the residuals of the intercooler faults are negative whilst that of the discharge valve leakage is positive. Furthermore, the two intercooler fault cases are also well separated, with the residual for the more severe one (IL2) being further from the baseline signal (BL) than is IL1. Of particular note, the residual of the combined fault case (IL2+VL) is closer to that of the discharge valve leakage fault, which can be explained by the fact that leakage of the discharge valve has a greater adverse influence on the performance of the compressor compared to the intercooler fault, as can be seen in Fig. 9.

It can be seen that the on-rotor acceleration is capable of diagnosing different leakage faults. In comparison, the traditional stator mounted accelerator can only detect localized faults. For measuring leakages, multiple vibration sensors may need to be mounted on the target leakage position, such as inlet or valve. This is because the rotor mounted accelerometer monitors the dynamic behavior of the crankshaft directly while the traditional stator mounted acceleration measurement can only detect localized vibration signals. This shows that on-rotor measurement can reduce the sensor numbers for condition monitoring.

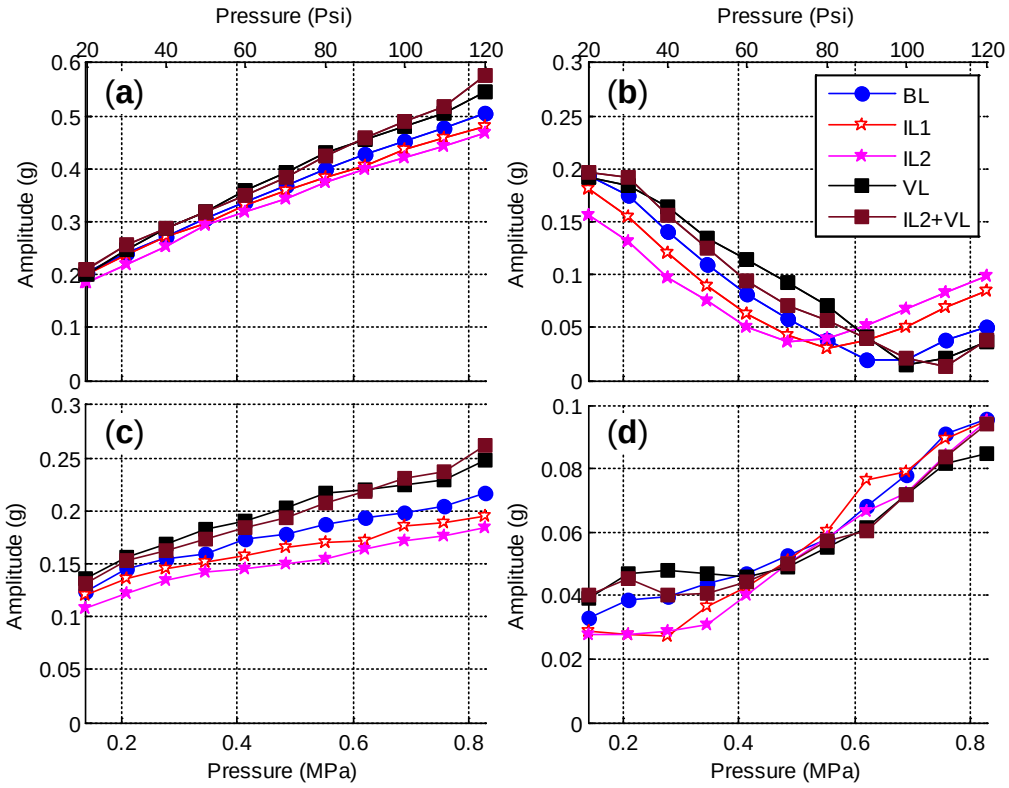


Fig. 10. Fundamental and harmonic amplitudes of the reconstructed acceleration signals vs. tank pressure. (a) fundamental frequency, (b) 2nd harmonic, (c) 3rd harmonic and (d) 4th harmonic.

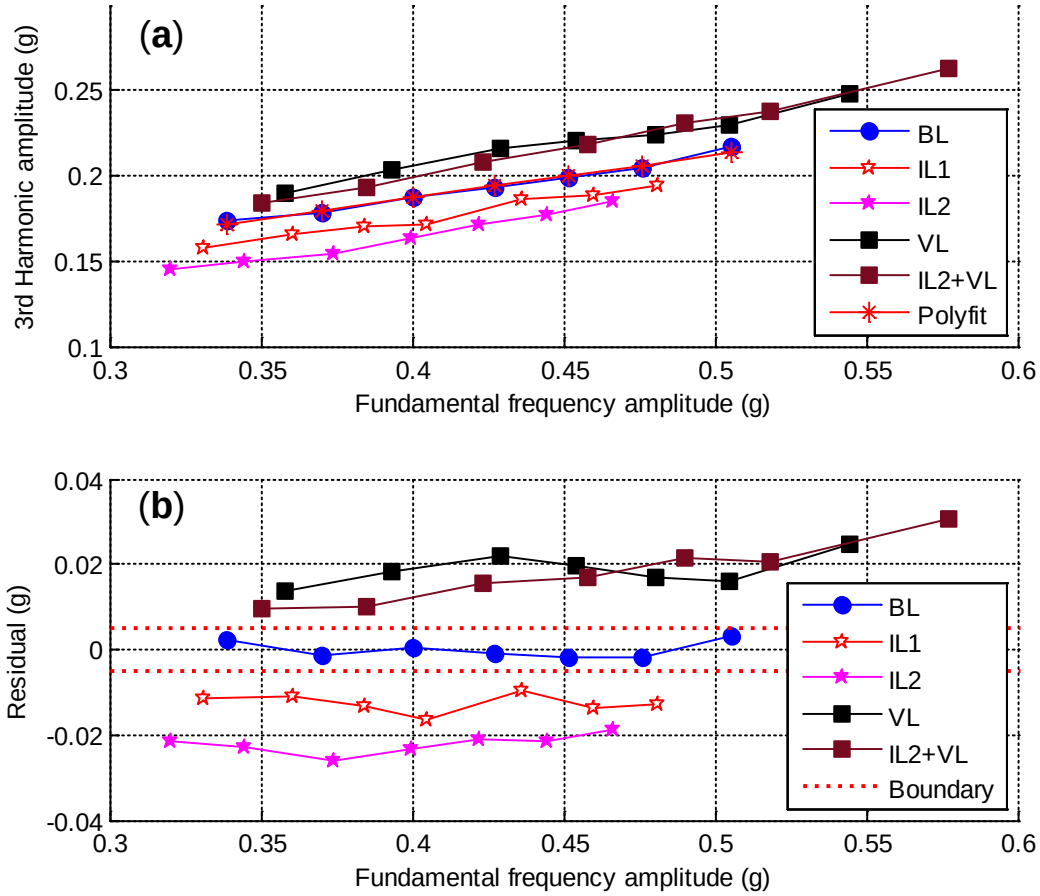


Fig. 11. Fault signal classification (a) 3rd harmonic vs. fundamental frequency (b) residual vs. fundamental frequency

# 5 Conclusions

In this paper, the tangential acceleration of a rotor is successfully reconstructed from the orthogonal outputs of a single on-rotor MEMS accelerometer. Using Monte-Carlo simulation, it has been shown that the reconstructed signal has good accordance with the original tangential acceleration.

With experimental study on a two-stage reciprocating compressor, it has been demonstrated that the reconstructed tangential acceleration is sufficiently accurate to reflect the discharge pressure of the compressor, and a range of simulated leakage faults can be detected and diagnosed from the relationship between the third harmonic and the fundamental component. Hence, by employing a single on-rotor MEMS accelerometer, with either two or three axes, the condition of the compressor can be monitored for a range of common fault types.

# Reference


[1] V. C. Gungor and G. P. Hancke, Industrial Wireless Sensor Networks: Challenges, Design Principles, and Technical Approaches, IEEE Trans. Ind. Electron., 56 (10) (2009) 4258 –4265.

[2] L. Hou and N. W. Bergmann, Novel Industrial Wireless Sensor Networks for Machine Condition Monitoring and Fault Diagnosis, IEEE Trans. Instrum. Meas., 61 (10) (2012) 2787 – 2798.

[3] Q. Sun, S. Patil, S. Stoute, N.-X. Sun, and B. Lehman, Optimum Design of Magnetic Inductive Energy Harvester and its AC-DC Converter, in Energy Conversion Congress and Exposition (ECCE), 2012 IEEE, (2012) 394–400.

[4] H. A. Thompson, Wireless Sensor Research at the Rolls-Royce Control and Systems University Technology Centre, in 1st International Conference on Wireless Communication, Vehicular Technology, Information Theory and Aerospace Electronic Systems Technology, 2009. Wireless VITAE 2009, (2009) 571–576.

[5] T. T. Toh, P. D. Mitcheson, A. S. Holmes, and E. M. Yeatman, A Continuously Rotating Energy Harvester with Maximum Power Point Tracking, J. Micromechanics Microengineering, 18(10), (2008) p. 104008.

[6] G. Manla, N. M. White, and M. J. Tudor, Numerical Model of a Non-Contact Piezoelectric Energy Harvester for Rotating Objects, IEEE Sens. J., 12 (6) (2012) 1785–1793.

[7] L. Arebi, F. Gu, and A. Ball, A Comparative Study of Misalignment Detection using a Novel Wireless Sensor with Conventional Wired Sensors, Journal of Physics: Conference Series, 364, (2012) p. 012049.

[8] L. Arebi, F. Gu, N. Hu, and A. Ball, Misalignment Detection Using a Wireless Sensor Mounted on a Rotating Shaft, in Proceedings of the 24th International Congress on Condition Monitoring and Diagnostics Engineering Management, (2011) 1289-1299.

[9] M. E. Elnady, A. Abdelbary, J. K. Sinha, and S. O. Oyadiji, FE and Experimental Modeling of On-shaft Vibration Measurement, in 15th International Conference on Aerospace Sciences & Aviation Technology, (2013) 1-18.

[10] M. E. Elnady, J. K. Sinha, and S. O. Oyadiji, Identification of Critical Speeds of Rotating Machines Using On-Shaft Wireless Vibration Measurement, J. Phys. Conf. Ser., 364, (2012) p. 012142.

[11] L. Baghli, J. F. Pautex, and S. Mezani, Wireless Instantaneous Torque Measurement, Application to Induction Motors, in 2010 XIX International Conference on Electrical Machines (ICEM), (2010) 1–6.

[12] A. Janota, V. Šimák, D. Nemec, and J. Hrbček, Improving the Precision and Speed of Euler Angles Computation from Low-Cost Rotation Sensor Data, Sensors, 15(3) (2015) 7016–7039.

[13] The United States National Electrical Manufacturers Association, the Association of Electrical Equipment and Medical Imaging Manufacturers, NEMA MG 1-2011. http://www.nema.org/Standards/Pages/Information-Guide-for-General-Purpose-Industrial-AC-Small-and-Medium-Squirrel-Cage-Induction-Motor-Standards.aspx, 2014.

[14] M. Feldman, Hilbert Transform Applications in Mechanical Vibration. Wiley, Chichester, 2011.

[15] M. Elhaj, F. Gu, A. D. Ball, A. Albarbar, M. Al-Qattan, and A. Naid, Numerical Simulation and Experimental Study of a Two-stage Reciprocating Compressor for Condition Monitoring, Mech. Syst. Signal Process., 22 (2), (2008) 374–389.

[16] Axivity Ltd., AX3 Datasheet. http://axivity.com/files/resources/AX3_Data_Sheet.pdf, 2015.